Energy-resolved STM mapping of C_{60} on metal surfaces: A theoretical study

Mario De Menech,[1,2] Ulf Saalmann,[1] and Martin E. Garcia[3]
[1]*Max-Planck-Institut für Physik komplexer Systeme, Nöthnitzer Straße 38, 01187 Dresden, Germany*
[2]*Theoretische Physik, Fachbereich Naturwissenschaften, Universität Kassel, Heinrich-Plett-Straße 40, 34132 Kassel, Germany*
[3]*Theoretische Physik, Fachbereich Naturwissenschaften, Universität Kassel and Center for Interdisciplinary, Nanostructure Science and Technology (CINSaT), Heinrich-Plett-Straße 40, 34132 Kassel, Germany*
(Received 23 November 2005; published 7 April 2006)

We present a detailed theoretical study of scanning tunneling imaging and spectroscopy of C_{60} on silver and gold surfaces, motivated by the recent experiments and discussion by [Lu *et al.* Phys. Rev. Lett. **90**, 096802 (2003); Phys. Rev. B **70**, 115418 (2004)]. The surface/sample/tip system is described within a self-consistent density-functional-theory-based tight-binding model. The topographic and conductance images are computed at constant current from a full self-consistent transport theory based on nonequilibrium Green's functions and compared with those simulated from the local density of states. The molecular orbitals of C_{60} are clearly identified in the energy resolved maps, in close correspondence with the experimental results. We show how the tip structure and orientation can affect the images. In particular, we consider the effects of truncated tips on the energy-resolved maps.

DOI: 10.1103/PhysRevB.73.155407 PACS number(s): 73.63.−b, 73.22.−f, 73.40.Gk

I. INTRODUCTION

Scanning tunneling microscopy (STM) was introduced to image surface structures in real space[1] and is nowadays used to obtain more complete information on the local electronic properties with the scanning tunneling spectroscopy (STS) technique. Its operation is based on the measurement of the tiny tunneling current flowing from a very sharp conducting tip to the surface when a bias voltage is applied. Images are obtained by recording the vertical displacement of the tip as it is moved across the surface while keeping the tunneling current constant with a precise feedback mechanism. If the current increases due to a protrusion on the surface, the tip is lifted to bring the current back to the set value, therefore revealing the topography of the substrate.

Tersoff and Hamann[2] have shown how the images do not only reflect the geometric structure of the surface, but also depend on the electronic density of states of the sample, which is identified, to a first approximation, with the differential conductance. This observation has opened the way to spectroscopic measurements with a spatial resolution which is by far not accessible by other surface science techniques. This capability is of particular interest in the study of adsorbates at surfaces, which can be addressed individually by the probe. The STS signal, on the other hand, is strongly influenced by the nature of the contact and the structure of the tip, and extraction of information on the physical and chemical properties of the measured sample is possible only with the support of electronic structure calculations with an atomistic description of the system.[3–5]

In this paper we discuss from a theoretical point of view the powerful combination between microscopy and spectroscopy which is peculiar of STM and STS. The accuracy of recent STM experiments on C_{60} monomers on metallic surfaces[6,7] represents a rigorous benchmark for any theoretical modeling of STM imaging and spectroscopy. Quite interestingly, energy-resolved mapping of the molecular orbitals of adsorbed C_{60} monomers has already been used as a control reference for even more sophisticated experiments[8]; similarly, we would like to discuss in detail STM and STS mapping of this system based on Green's function methods, in view of the investigation of adsorbed molecules and clusters[9] which have not yet been experimentally characterized with this technique. Topographic and energy-resolved maps are computed with a realistic model of the STM probe, with the simulation of the tip trajectory over constant current surfaces; the effects of the tip structure on the rendered images are illustrated in detail, showing that truncated tips may duplicate the characteristic features depending on the orientation of the topmost atoms with respect to the sample. Also, we refine previous calculations based solely on the local density of states (LDOS) of the supported molecule.[6,7] We confirm that the images obtained from the LDOS can effectively approximate the patterns observed in the STS maps, with the additional piece of advice that the simulated probe trajectory should be taken at the correct distance from the molecule.

The paper is organized as follows. The theoretical framework is briefly reviewed in Sec. II. The experienced reader may skip this part and move directly to the results in Sec. III. Equilibrium electronic properties of the supported C_{60} are discussed in Sec. III A, while the calculations based on transport theory are in Sec. III B, extended by simulation of topographic and spectroscopic images with different types of tips in Sec. III C. Finally, in Sec. III D we specify how STS maps can be modeled using the local density of states.

II. THEORY

We consider a fully atomistic description of the surface, molecule, and STM probe. The geometry of substrate and the STM electrode are fixed from bulk properties—i.e., surface relaxation effects are neglected—and the structure of the molecule is assumed to remain unchanged after adsorption. The transport properties are computed with a microscopic approach using nonequilibrium Green's functions, and the

electronic structure is modeled within a single-particle picture, based on a self-consistent tight-binding (TB) model which is parametrized from density functional theory (DFT).

A. TB-DFT model

Electron wave functions are approximated by an expansion in an atomiclike orbital basis,[10] which is determined by solving the Kohn-Sham equations of the individual atoms within the local-density approximation (LDA). The TB Hamilton matrix expressed in the localized basis consists only of two-center integrals which can be obtained exactly by using Slater-type functions for the atomic orbitals. This scheme is refined to include charge self-consistency by expanding the DFT energy functional to the second order in the charge-density fluctuations.[11,12] Such an expansion leads to the appearance of an additional term to complete the TB Hamiltonian that contains the contribution of the net atomic charges on the local effective potential. Like in a full DFT calculation, self-consistency is obtained with iterative methods, such that the local density, given by the sum of the (approximated) Kohn-Sham eigenfunctions, is consistent with the effective potential. The main advantage of this approach lies in its simplicity and computational efficiency, while basic key effects like charge transfer and redistribution are still handled correctly.

B. Equilibrium electronic properties of adsorbates

Inglesfield[13,14] introduced the concept of embedding potential to perform real-space electronic structure calculations in a domain surrounding impurities or defects in an otherwise perfect crystal. The form of the embedding potential is derived from the Green's function of the solid and is included in an effective Schrödinger equation, to be solved only in the region of interest, ensuring the correct matching of the solutions with the wave function in the rest of the solid. A complementary approach considers the defect as a perturbation of the ideal system and was first proposed by Williams, Feibelman, and Lang.[15] A localized atomic orbital basis $\{|\varphi_\mu(r)\rangle\}$ is introduced to represent in matrix form the Hamiltonian $\tilde{\mathbf{H}}$ and the (retarded) Green's function $\tilde{\mathbf{G}}$, defined by

$$[(E+\mathrm{i}\eta)\tilde{\mathbf{S}}-\tilde{\mathbf{H}}]\tilde{\mathbf{G}}(E)=\mathbb{1}, \quad \eta\to 0^+, \tag{1}$$

$\tilde{\mathbf{S}}\equiv S_{\mu\nu}=\langle\varphi_\mu|\varphi_\nu\rangle$ being the overlap matrix. The indices for matrices with a tilde run over the atomic orbitals of the surface and the cluster.

Measurable quantities can be computed directly from the Green's function; for example, from the spectral density matrix

$$A_{\mu\nu}(E)=-\frac{2}{\pi}\,\mathrm{Im}[G_{\mu\nu}(E)] \tag{2}$$

(the factor of 2 is explicity included to point out that we consider a spin-unpolarized system), it is possible to compute the local density of states

$$\rho(\mathbf{r},E)=\sum_{\mu\nu}A_{\mu\nu}(E)\varphi_\mu(\mathbf{r})\varphi_\nu(\mathbf{r}) \tag{3}$$

and therefore the density

$$n_{\mathrm{eq}}(\mathbf{r})=\int_{-\infty}^{E_\mathrm{F}}\mathrm{d}E\rho(\mathbf{r},E), \tag{4}$$

where E_F is the Fermi level (degenerate case).

The localized basis allows to translate the cluster-surface partitioning of the system into the block structure for the overlap, Hamilton, and Green's function matrices of Eq. (1). The Green's function of the isolated cluster, $\mathbf{G}^0$, is modified by the presence of the surface and can be obtained from the solution of the Dyson equation

$$\mathbf{G}=\mathbf{G}^0+\mathbf{G}^0\boldsymbol{\Sigma}\mathbf{G}, \tag{5}$$

where $\mathbf{G}$ refers to the Green's function of the "embedded" cluster and $\boldsymbol{\Sigma}$ is the matrix analog[16] of Inglesfield's embedding potential. Note that, in contrast to Eq. (1), all matrices in Eq. (5) are defined for orbitals at the cluster only. $\boldsymbol{\Sigma}$ can be expressed as a self-energy

$$\boldsymbol{\Sigma}(E)=\mathbf{V}(E)\mathbf{G}_\mathrm{s}^0(E)\mathbf{V}^\dagger(E), \tag{6}$$

thereby including the scattering processes due to the interaction with the surface, given by the combination of the unperturbed surface Green's function $\mathbf{G}_\mathrm{s}^0$ and the tunneling matrix $\mathbf{V}=E\mathbf{S}_\mathrm{cs}-\mathbf{H}_\mathrm{cs}$. $\mathbf{S}_\mathrm{cs}$ and $\mathbf{H}_\mathrm{cs}$ are the overlap and Hamilton matrices between orbitals at the surface and cluster. For an orthogonal basis $\mathbf{S}_\mathrm{cs}$ would vanish and $\mathbf{V}$ would be independent of the energy E.

Having chosen a localized orbital basis, only a limited number of elements in the tunneling matrix are different from zero and $\mathbf{G}_\mathrm{s}^0$ needs to be evaluated just for the surface atoms which are within a finite distance from the supported cluster. The two-dimensional periodic structure of the surface allows us to reduce the corresponding overlap and Hamilton matrices in a block-diagonal form, based on the transformation to the two-dimensional momentum space. The surface is then partitioned in a series of adjacent layers, and the Green's function for the first layer, the needed submatrix of $\mathbf{G}_\mathrm{s}^0$, can be efficiently computed for any $\mathbf{k}$ point using recursive methods.[17] The conversion to the real-space representation is finally obtained by integrating over a finite number of $\mathbf{k}$ values in the first Brillouin zone (we sampled over a regular grid with at least 1600 points).

Charge self-consistency requires that the effective potential entering in the system Hamiltonian lead to a charge density which generates the same effective potential. It is obtained with an iterative scheme, by computing the local charge densities from $\mathbf{G}$, to be fed into the local effective potential of the cluster Hamiltonian,[12] therefore leading to a new cluster Green's function, which provides the density for the next iteration, until convergence is reached. The integral of Eq. (4) is evaluated most efficiently taking advantage of the analytic structure of the Green's function, with a contour integration in the upper complex plane.[15,18] Since the substrate is described as an ideal surface, the effect of screening due to the charge redistribution in the metal is achieved by

including image charges, which generate an external field acting on the cluster region and provide the correct boundary conditions for the Poisson equation, such that the electrostatic potential on the first atomic plane of the surface is uniform and set to zero.

C. Transport

The expression for the density in Eq. (4) is valid only in equilibrium conditions. When the sample is probed with an STM tip at nonzero bias V, the local charge is obtained from the correlation function $\mathbf{G}^<$ defined by[19]

$$\mathbf{G}^< = \mathbf{G}\mathbf{\Sigma}^<\mathbf{G}^\dagger, \tag{7}$$

where the lesser self-energy

$$\mathbf{\Sigma}^< = \mathrm{i}[f(E-\mu_s)\mathbf{\Gamma}^s + f(E-\mu_t)\mathbf{\Gamma}^t] \tag{8}$$

depends on the chemical potentials $\mu_s = E_F$ and $\mu_t = \mu_s + |e|V = E_F + |e|V$ of the surface and tip, respectively. In Eq. (8), f is the Fermi function and $\mathbf{\Gamma}^s$ and $\mathbf{\Gamma}^t$ are the broadening matrices. They include the interaction with the surface and the tip through the respective self-energies

$$\mathbf{\Gamma}^s = \mathrm{i}[\mathbf{\Sigma}^s - [\mathbf{\Sigma}^s]^\dagger], \quad \mathbf{\Gamma}^t = \mathrm{i}[\mathbf{\Sigma}^t - [\mathbf{\Sigma}^t]^\dagger], \tag{9}$$

where the cluster-tip self-energy $\mathbf{\Sigma}^t$ is defined as for the surface case in Eq. (6). The nonequilibrium analog of Eq. (4) reads

$$n(\mathbf{r},V) = \frac{1}{\pi \mathrm{i}}\int_{-\infty}^{\infty} \mathrm{d}E G^<_{\mu\nu}(E,V)\varphi_\mu(\mathbf{r})\varphi_\nu(\mathbf{r}) \tag{10}$$

and enters in self-consistent relaxation of the electronic charge in the cluster, as for the equilibrium case. The correlation function—therefore the nonequilibrium density—depends directly on the applied bias V due to the shift of the tip chemical potential μ_t. The numerical procedure for the computation of the electron density splits the integral in Eq. (10) into equilibrium and nonequilibrium contributions, exploiting the same contour integration used to evaluate the equilibrium density.[18]

In the crudest approximation, the tip electrode is assumed to be a flat metal surface, to be treated exactly like the one supporting the sample. The boundary conditions for the Poisson equation are that the surfaces of the two electrodes have a constant uniform potential differing by the bias voltage, and the correct electrostatics is obtained using a series of image charges on both sides. This choice of boundary conditions implies that $\mathbf{G}^<$ depends on the external potential generated by the two electrodes, which enters both in the cluster and tunneling Hamiltonians and therefore determines the cluster Green's function, now $\mathbf{G}(E,V)$, and the broadening matrices. Realistic tips are easily included in the model by considering the tip atoms as part of the cluster, which will then just be a larger sample sandwiched between the two parallel electrodes. The arrangement of the tip atoms was assumed to be consistent with the crystal structure of the underlying ideal surface.

In the case of coherent transport—i.e., when there is no inelastic scattering within the sample—the stationary current is given by the simple formula[20]

$$I = \frac{2e}{h}\int_{-\infty}^{\infty} \mathrm{d}E T(E,V)[f(E-\mu_t) - f(E-\mu_s)], \tag{11}$$

where T is the transmission function[21]:

$$T(E,V) = \mathrm{Tr}[\mathbf{G}(E,V)\mathbf{\Gamma}^s(E)\mathbf{G}^\dagger(E,V)\mathbf{\Gamma}^t(E-|e|V)]. \tag{12}$$

The effects of scattering processes within the conductor due to electron-electron or electron-phonon interactions can be treated consistently within the nonequilibrium Green's function framework by adding the corresponding self-energy terms,[19,20] but will not be considered in this paper. Electron-electron interactions are incorporated here at a mean-field level, which does not cause incoherent effects.[19]

III. RESULTS

For the calculations presented below, C_{60} was placed with different orientations on Ag(111) and Au(111) surfaces at a distance of 2.4 Å, consistent with the value obtained from first-principles calculations for monolayers.[22] The structure of the supported molecule was not relaxed from the free configuration.

A. Total DOS of supported cluster

Figure 1 shows the total DOS of C_{60} for three different orientations on Au(111) and Ag(111) surfaces. For each of these orientations it was observed that the number and position of the peaks remain unchanged as the molecule is translated in the plane parallel to the surface, showing that in both cases there is no chemical bonding with the substrate. For C_{60} on Ag(111), besides the broadening and splitting of the levels of the free molecule due to the interaction with the surface, we observe a shift of +0.7 eV associated with a net transfer of 0.3 electrons to the molecule, as given by the Mulliken charge analysis. In the case of the Au substrate there is almost no charge transfer (0.01 electrons), which leaves the position of the free-cluster energy levels unchanged. Also, we observe that the LUMO peak for the Ag case appears much more broadened than for Au, with its lower-energy tail approaching the Fermi level, similarly to what was observed by other DFT calculations.[6,7] The energy difference $E_{LUMO} - E_{HOMO}$ is equal to 2.0 eV in both cases, while the experimental gap is 2.0 eV for Ag(100) and 2.7 eV for Au(111).[6,7] The discrepancy is to be imputed mainly to the intrinsic limits of LDA eigenvalues as a representation of electronic excitation energies.

B. Transport calculations

For the calculation of the conductance as a function of energy and of the current–voltage characteristics we consider the combination C_{60}/tip as a single conductor placed between two parallel, infinite, ideal surfaces (Fig. 2). This way of partitioning the system is convenient since the Green's

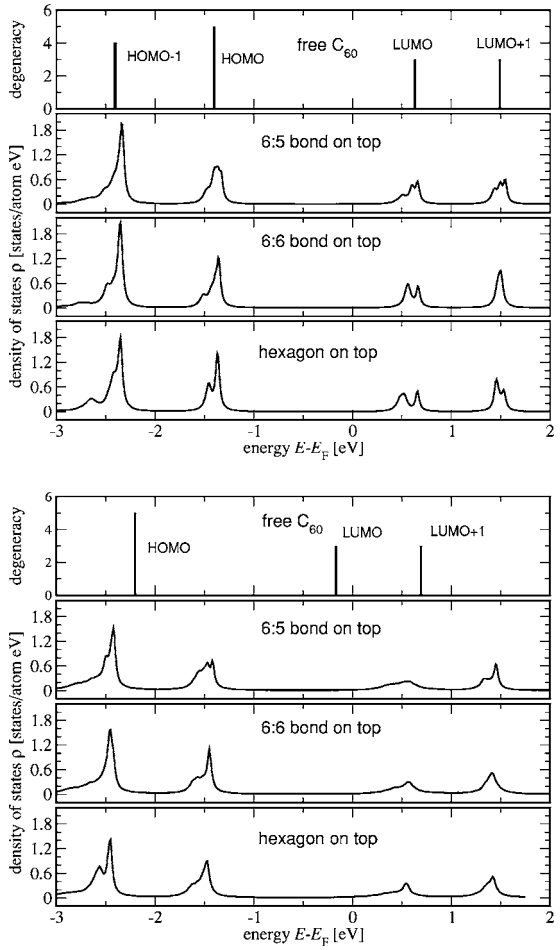

FIG. 1. Total DOS $\rho(E)$ of C_{60} with different orientations on Au(111) (left column) and Ag(111) (right column). The top figure shows the position of the highest occupied molecular orbital (HOMO), lowest unoccupied molecular orbital (LUMO), and LUMO+1 orbitals for the free molecule relative to the Fermi level of the Au and the Ag surface, respectively.

function of the surfaces can be computed efficiently (see Sec. II B). We choose Au as element for our probe, which, in contrast to the transition metals used in experiments, has a fairly uniform DOS near the Fermi level, without any contribution from the d states. This choice allows us to single out the effects of the tip atomic structure on the calculated maps. We will use the term conductance for the quantity

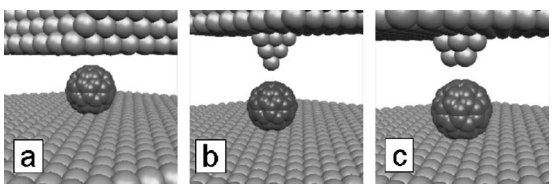

FIG. 2. Representation of the junction formed by the surface/C_{60}/tip/electrode. (a) flat electrode (no tip atom), (b) sharp tip (single atom at tip end), and (c) truncated tip (three atoms at tip end).

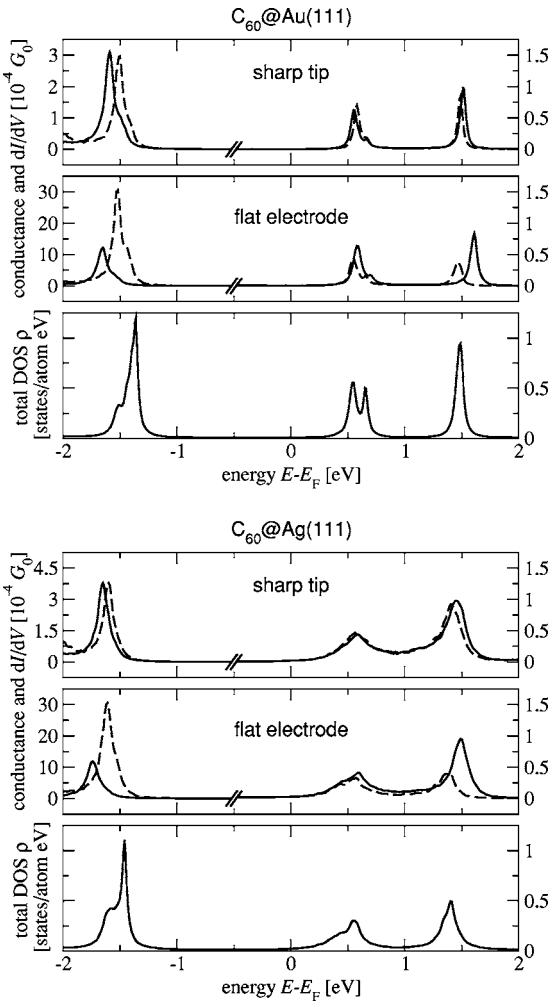

FIG. 3. Comparison of spectral density, conductance, and differential conductance for C_{60} on Au(111) and Ag(111) surfaces. Bottom panels: total DOS $\rho(E)$. Center and top panels: conductance G (dashed lines) and differential conductance dI/dV (solid lines) for a probe made with the flat electrode [Fig. 2(a)] or the sharp tip [Fig. 2(b)], respectively, each placed at 5.5 Å from the top of the molecule. Note the different scales for the peaks of G and dI/dV for $E-E_F<-0.5$ eV and $E-E_F>-0.5$ eV, respectively ($G_0=2e^2/h$).

$$G(E) = G_0 T(E, V=0), \tag{13}$$

with $G_0=2e^2/h$ and $T(E,V)$ defined in Eq. (12); the transmission function is therefore computed from the self-consistent Hamiltonian of the system at zero bias. In contrast, the differential conductance dI/dV is obtained from the derivative of the total current (11) for each bias value and will be sensitive to the external field, leading most notably to shifts of the energy levels and therefore to the peak positions.

In Fig. 3 we compare the spectral density $\rho(E)$ of the supported molecule with the conductance G and differential conductance dI/dV curves as a function of the bias. The latter two are computed both for a flat electrode [Fig. 2(a)] and a sharp tip consisting of ten atoms [Fig. 2(b)]. Conductance and total DOS peaks appear at the same position. However, the relative height of the peaks changes dramatically; when switching to the sharp tip, the conduction through the

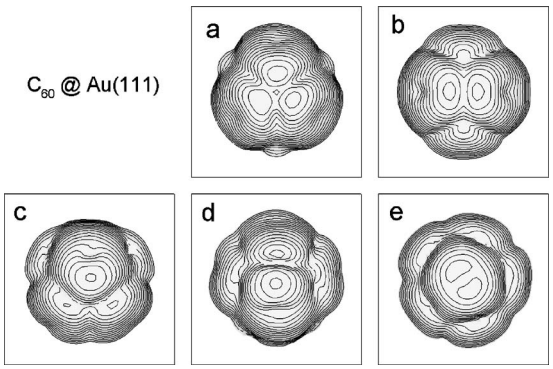

FIG. 4. Computed topographic images of C_{60} on Au(111) with different orientations; the topmost features are (a) a hexagon ring, (b) a 6:6 bond, (c) a 5:6 bond, (d) an apex atom, and (e) a pentagon ring. Current was set to 77.5 pA, the bias to +1.8 V. The size of each frame is 20×20 Å^2. Compare to Fig. 1 in Lu *et al.* (Ref. 7).

HOMO level drops by about an order of magnitude, while for the LUMO and LUMO+1 there is a slight increase in the conductance.

At finite bias, the external field modifies the local charge distribution and displaces the peaks of the differential conductance with respect to the equilibrium energy levels. Due to the large separation between the tip and C_{60} molecule, these shifts can be appreciated only at large biases. A similar behavior is observed for a sharp tip, which in this case was placed centrally above the C_{60} molecule. Here, as well, the HOMO conducts current better than the LUMO and LUMO+1 states; the difference in conductance, however, is attenuated. This behavior depends in fact on the position of the tip and will be discussed in the following section.

C. STM and STS imaging with realistic tip models

1. Normal maps

We first model STM and STS imaging with a sharp tip [Fig. 2(b)]. The tip is moved on a three-dimensional finite-element mesh placed above the molecule, with a grid spacing of 0.5 Å. For each position the current I and the differential conductance dI/dV are computed using Eq. (11). The constant-current isosurface is obtained by interpolation and provides the topographic image of the molecule at the given voltage bias, as shown in Figs. 4(a)–4(e) for five different orientations. The bias is set to +1.8 V, and the pentagon rings of the C_{60} bulge out in a doughnutlike shape from the spherical structure of the molecule, allowing the direct identification of its orientation on the surface.

Based on the topographic scan of C_{60} with a 6:6 bond (a carbon bond shared by two hexagon rings) as a topmost feature reported in Fig. 4(b), we show in Fig. 5 conduction curves for six tip positions. Heights and shapes of the peaks vary considerably as the tip is moved over the molecule, and we also observe slight shifts in their position in the energy scale, induced by the changes in the local electric field surrounding the STM probe.

The strong spatial dependence of the conductance allows to construct energy-resolved maps (Fig. 6) to represent the

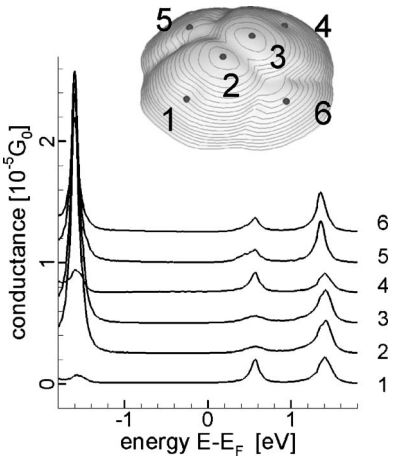

FIG. 5. Dependence of calculated STS spectra on the tip position for the C_{60} molecule at the Ag(111) surface with a 6:6 bond on the top. The spectra are shifted along the vertical axis for clarity.

states associated with each peak. The simulated STS maps are rendered by displaying the computed dI/dV values with a contour plot on the three-dimensional tip trajectory, which is then projected on the two-dimensional plane of view, which in this paper will always be parallel to the metal surface. The gray-scale code associates bright areas to high conductance, dark areas to low conductance.

The structure of the HOMO, LUMO, and LUMO+1 molecular orbitals is clearly visible in the calculated maps re-

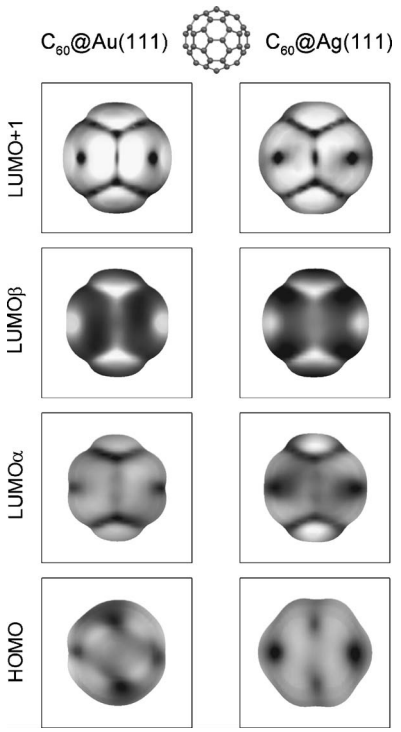

FIG. 6. Energy-resolved maps of molecular orbitals for C_{60} on Au(111) and Ag(111) surfaces with 6:6 bond as the uppermost feature. The maps for HOMO, LUMOα, LUMOβ, and LUMO+1 are obtained at −1.32 eV, 0.40 eV, 0.64 eV, and 1.46 eV for Au(111) and at −1.40 eV, 0.30 eV, 0.55 eV, and 1.36 eV for Ag(111). The size of each frame is 20×20 Å^2.

ported in Fig. 6, similarly to what was observed in experiments (cf. Fig. 3 of Lu *et al.*[6] and Fig. 3 of Lu *et al.*[7]). In particular, the LUMO level appears to be composed of two orbitals LUMOα and LUMOβ, having a complementary spatial distribution of the conductance. This pattern was observed in experiments[6] for the Ag(100) surface, where the LUMO peak displays a marked splitting of 0.4 eV. By calculating maps for two energies (0.40 and 0.64 eV) within the LUMO peak, we are able to extract two conjugate LUMO images also for the case of the Au substrate, which points out that the two states simply arise from the lifting of the degeneracy of the LUMO level of the free molecule due to the contact with the surface. We therefore conclude that the splitting was not observable in the case of the Au surface[7] due to the limits in resolution for STM spectroscopy. What remains still unclear is the reason why the states are so well separated in the experiments performed with the Ag(100) substrate.[6] The main clue is the large charge transfer to the molecule, compared to the neutrality for the case of the Au surface, which may induce a deformation in the molecule therefore lifting degeneracy of the LUMO level.[6]

2. Abnormal maps

In order to investigate the sensitivity of the energy-resolved maps to the structure of the probe, we considered a truncated tip, having three atoms at its end [Fig. 2(c)]. Figure 7 shows the calculated images for C_{60} with two different orientations of the tip [columns (a) and (b)], whose position is given by the center of mass of the three end atoms. At all energies, the overall shape of the maps reflects the triangular arrangement of the three atoms at the end of the truncated tip; a rotation of the probe around the axis normal to the surface rotates the image of the molecule [compare columns (a) and (b) of Fig. 7], despite the fact that the position of the molecule remains unchanged. For the LUMO+1 level we observe that the bright rings corresponding to the pentagons in the C_{60} are duplicated, which should be linked with the presence of two adjacent atoms in the triangle. For the orientation (a) the alignment of the tip is such that this sort of dichroism is present only for the left side of the maps, while when the tip moves to the right side only one atom remains closer to the molecule and the single bright ring is recovered. A similar behavior can be noticed also for LUMOα and the complementary map LUMOβ.

Most features described so far can be roughly explained assuming that, like in the case of the sharp tip, at every position of the simulated scan tunneling occurs between the sample and only one atom of the probe: namely, the one closest to the adsorbed molecule. The main difference is that for the truncated tip such atom is not always the same, which leads to the dichroism mentioned above. Only in the central region may all three atoms contribute equally; the bright spot appearing right at the center of the LUMO+1 map in Fig. 7 appears precisely because of the rise in conductance given by the sum of the tunneling currents through the three end atoms. We also note that, compared to the well-contrasted images of Fig. 5, the coherent structure of the HOMO level becomes less evident when imaging with the blunt tip. In this case, the coarser nature of the probe sensibly changes the trajectory of the tip, which therefore moves over a surface having a lower corrugation, borrowing form the terminology used for flat surfaces. The tunneling current involves more than one atom of the tip, hindering the resolution of the fine structure of the HOMO orbital.

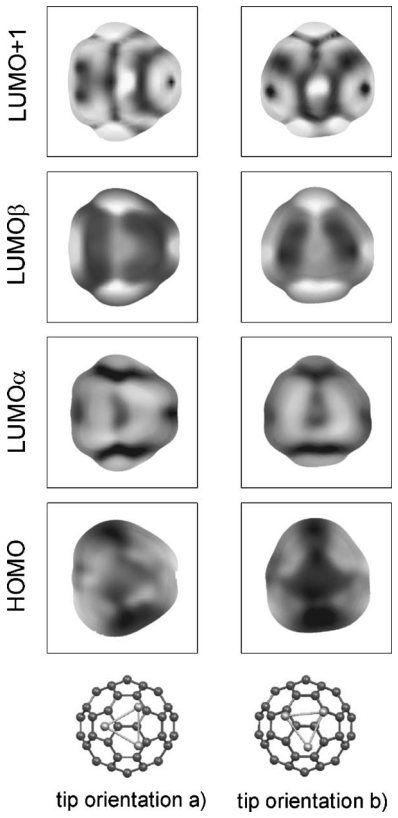

FIG. 7. Energy-resolved maps with a truncated tip of C_{60} on Au(111) with the 6:6 bond on top (compare 6). Column (a): tip in the reference position. Column (b): tip rotated by 23° around the axis normal to the surface. The orientation of the three atoms at the bottom of the STM probe is reported for each series of images. The size of each frame is 20×20 Å^2.

These results clearly demonstrate how the details of the energy-resolved maps of C_{60} can reveal the structure and orientation of the STM tip and how this kind of analysis could serve as a tool to characterize the properties of the probes used in experiments.

D. STM and STS imaging from LDOS

Within Tersoff-Hamann theory,[2] the STM topographic and spectral images are modeled assuming that the current at bias V is proportional to the spatially resolved density of states:

$$I(\mathbf{r},V) \propto \int_{E_F}^{E_F+|e|V} \mathrm{d}E\rho(\mathbf{r},E). \tag{14}$$

Equation (14) allows us to calculate the tip trajectory, based on the assumption that the convolution effects due to the tip shape and states can be neglected. The local differential conductance $\mathrm{d}I(\mathbf{r},V)/\mathrm{d}V \propto \rho(\mathbf{r},E)$ can be projected onto the isocurrent surface to simulate the experimental procedure

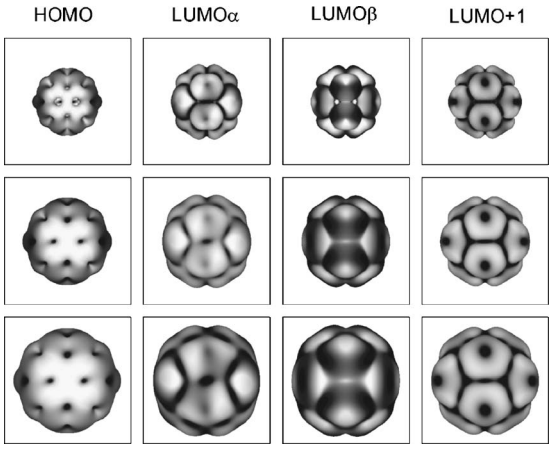

FIG. 8. Energy-resolved maps from the LDOS for C_{60} on Ag(111) with a 6:6 bond on top. The three columns from left to right show simulated tip trajectories which are approximately 2, 3.5, and 5 Å away from the C_{60}. The size of each frame is 20×20 Å^2.

followed to measure STS maps. The frames in Fig. 8 show that the patterns in the molecular orbitals discussed so far can be reproduced with the LDOS, provided that the calculated tip trajectory is placed far enough from the molecule. The standard choice is in fact to consider the LDOS at a few Å from the atoms of the sample, and we verified that the peculiar LUMOα and LUMOβ images can be obtained only considering isosurfaces at 3.5–5 Å from the C_{60} molecule.

IV. SUMMARY

We have presented a detailed numerical investigation of STM topographic and energy-resolved mappings of C_{60} on gold and silver surfaces. The transport calculations are based on nonequilibrium Green's function methods, with a DFT-based tight-binding model. Self-consistency allows us to study the charge redistribution of the molecule due to the presence of the supporting surface, as well as due to external field generated by the voltage difference between the substrate and STM probe.

We have discussed the importance of realistic models for the tip, using a sharp tip, we could perfectly reproduce recently measured energy-resolved maps for C_{60} on metal surfaces.[6,7] The images are obtained by projecting the contour plot of the differential conductance mapped on the three-dimensional surface described by the tip as it scans the sample with a fixed tunneling current. Images of a similar quality can be obtained from the LDOS using Tersoff-Hamann theory to calculate the conductance if the simulated constant-current surface is sufficiently far from the cluster (here more than 3 Å).

Additionally, we have modeled the STM and STS mapping with a truncated tip and described the appearance of abnormal images that allow us to reconstruct the structure of the probe by direct comparison with the ideal maps. We finally suggest that this procedure could be used to gauge the properties of the STM probes, which is generally unknown in STM experiments.

ACKNOWLEDGMENTS

We acknowledge financial support by the Deutsche Forschungsgemeinschaft (DFG) through the priority program SPP 1153 "Clusters in contact with surfaces: Electronic structure and magnetism."

[1] G. Binnig, H. Rohrer, C. Gerber, and E. Weibel, Phys. Rev. Lett. **49**, 57 (1982).
[2] J. Tersoff and D. R. Hamann, Phys. Rev. B **31**, 805 (1985).
[3] S. Corbel, J. Cerdá, and P. Sautet, Phys. Rev. B **60**, 1989 (1999).
[4] D. Drakova, Rep. Prog. Phys. **64**, 205 (2001).
[5] J. M. Blanco, C. Gonzalez, P. Jelinek, J. Ortega, F. Flores, and R. Perez, Phys. Rev. B **70**, 085405 (2004).
[6] X. Lu, M. Grobis, K. H. Khoo, S. G. Louie and M. F. Crommie, Phys. Rev. Lett. **90**, 096802 (2003).
[7] X. Lu, M. Grobis, K. H. Khoo, S. G. Louie, and M. F. Crommie, Phys. Rev. B **70**, 115418 (2004).
[8] M. Grobis, K. H. Khoo, R. Yamachika, X. Lu, K. Nagaoka, S. G. Louie, M. F. Crommie, H. Kato, and H. Shinohara, Phys. Rev. Lett. **94**, 136802 (2005).
[9] M. De Menech, U. Saalmann, and M. E. Garcia, Appl. Phys. A: Mater. Sci. Process. **82**, 113 (2006).
[10] D. Porezag, T. Frauenheim, T. Kohler, G. Seifert, and R. Kaschner, Phys. Rev. B **51**, 12947 (1995).
[11] U. Saalmann, Ph.D. thesis, Technische Universität Dresden, 1997.
[12] M. Elstner, D. Porezag, G. Jungnickel, J. Elsner, M. Haugk, T. Frauenheim, S. Suhai, and G. Seifert, Phys. Rev. B **58**, 7260 (1998).
[13] J. E. Inglesfield, J. Phys. C **14**, 3795 (1981).
[14] J. E. Inglesfield, J. Phys. F: Met. Phys. **11**, L287 (1981).
[15] A. R. Williams, P. J. Feibelman, and N. D. Lang, Phys. Rev. B **26**, 5433 (1982).
[16] G. A. Baraff and M. Schlüter, J. Phys. C **19**, 4383 (1986).
[17] M. Lopez-Sancho, J. M. Lopez-Sancho, and J. Rubio, J. Phys. F: Met. Phys. **15**, 851 (1985).
[18] M. Brandbyge, J.-L. Mozos, P. Ordejon, J. Taylor, and K. Stokbro, Phys. Rev. B **65**, 165401 (2002).
[19] S. Datta, *Electronic Transport in Mesoscopic Systems*, Cambridge Studies in Semiconductor Physics and Microelectronic Engineering, Vol. 3 (Cambridge University Press, Cambridge, England, 1995).
[20] Y. Meir and N. S. Wingreen, Phys. Rev. Lett. **68**, 2512 (1992).
[21] Y. Xue, S. Datta, S. Hong, R. Reifenberger, J. I. Henderson, and C. P. Kubiak, Phys. Rev. B **59**, R7852 (1999).
[22] L.-L. Wang and H.-P. Cheng, Phys. Rev. B **69**, 165417 (2004).